The Astronomical Journal, 132:242–252, 2006 July

74 MHz DISCRETE H II ABSORPTION REGIONS TOWARD THE INNER GALAXY

Michael E. Nord
Naval Research Laboratory, Remote Sensing Division, Code 7263, 4555 Overlook Avenue SW, Washington, DC 20375-5351; and Computational Physics, Inc., 8001 Braddock Road, Suite 210, Springfield, VA 22151; michael.nord@nrl.navy.mil

P. A. Henning and R. J. Rand
Department of Physics and Astronomy, University of New Mexico, 800 Yale Boulevard NE, Albuquerque, NM 87131; henning@phys.unm.edu, rjr@phys.unm.edu

and

T. Joseph W. Lazio and Namir E. Kassim
Naval Research Laboratory, Remote Sensing Division, Code 7213, 4555 Overlook Avenue SW, Washington, DC 20375-5351; joseph.lazio@nrl.navy.mil, namir.kassim@nrl.navy.mil
Received 2005 August 17; accepted 2006 March 2

ABSTRACT

At low radio frequencies ($\nu \lesssim 100$ MHz), classical H II regions may become optically thick (optical depth $\tau \geq 1$) and can be observed as discrete absorption regions against the Galactic nonthermal background emission created by Galactic cosmic-ray electrons spiraling around magnetic fields. However, the historically poor angular resolution (>30′) of previous low-frequency surveys has limited such observations to the largest and nearest H II regions. The significantly enhanced resolution and surface brightness sensitivity of the 74 MHz system on the Very Large Array now allow for the detection of absorption regions on scale sizes of just a few arcminutes that can be readily identified with many more H II regions previously cataloged in emission at higher frequencies. These absorption measurements directly constrain the brightness temperature of the cosmic-ray synchrotron emission emanating from behind the H II regions based on reasonable physical assumptions. Many such observations could be used to map out the three-dimensional cosmic-ray emissivity in the Galaxy without resorting to a priori assumptions about Galactic structure. This measurement is unique to low-frequency radio astronomy. In this work we present 74 MHz observations in the region $26° > l > -15°$, $-5° < b < 5°$; report the detection of 92 absorption features associated with known H II regions; and derive the brightness temperature of the Galactic cosmic-ray electron synchrotron emission emanating from the column behind these regions. For the 42 H II regions with known distances, the average emissivity of the column behind the H II region is derived. The 74 MHz emissivity values range between 0.3 and 1.0 K pc^{-1} for a model assuming uniform distribution of emissivity. Methods for using this type of data to model the three-dimensional distribution of cosmic-ray emissivity and the possibility of using this method to break the H II region kinematic distance degeneracy are discussed.

Key words: cosmic rays — H II regions — ISM: magnetic fields — radio continuum: general

Online material: machine-readable table

1. INTRODUCTION

At low frequencies, the Galactic background emissivity[1] is dominated by the nonthermal synchrotron radiation caused by cosmic-ray (CR) electrons interacting with the Galactic magnetic field. Although CRs were first observed nearly 90 years ago (Hess 1919) and are thought to represent a significant fraction of the energy density of interstellar space ($\sim$1.8 eV cm^{-3}; Webber 1998), their origin, distribution, and energy spectrum are still only partly understood. This is in part because although multiple tracers of CR electrons exist, they typically produce line-of-sight integrated measurements only. One must then assume a model of Galactic structure to derive the three-dimensional distribution of the CR emissivity.

It is now widely accepted that Galactic supernova remnants (SNRs) are responsible for the acceleration of CRs of energies up to at least 10^{15} eV (e.g., Jones et al. 1998), a view supported by the detection of nonthermal X-ray (Koyama et al. 1995) and γ-ray (Aharonian et al. 2005) emission from SNRs. The typical energy of the CR electron population being detected at 74 MHz may be calculated by assuming that the CR energy spectrum is a power law of the form $N(E) \propto E^{-2.5}$ (Webber 1993a). Relativistic electrons with energy E emit maximum power at a frequency of

$$\nu = (16\ \text{MHz}) B(\mu\text{G}) E^2(\text{GeV})$$

(Rockstroh & Webber 1978), resulting in a typical energy of $\sim$0.4 GeV at 74 MHz for a reasonably assumed mean Galactic magnetic field strength of 5 μG (e.g., Rand & Kulkarni 1989). Therefore, SNRs are the most likely progenitor of many if not most of the CR electrons in the energy range we are sensitive to in this work.

After initial acceleration in SNR shock fronts, propagation of CRs may occur through diffusion, convection, or other mechanisms (e.g., Duric 1999; Lisenfeld & Völk 2000; Webber 1990; Longair 1990; Cesarsky 1980), but a central problem in placing

[1] Emissivity is a measure of intensity per unit length (SI units are W m^{-3} Hz^{-1} sr^{-1}). As equivalent brightness temperature is used in this work, the units used are K pc^{-1} and the symbol ε is used to denote it.

observational constraints on all CR acceleration and propagation models is the lack of distance information available in CR tracer observations.

Observations of H II regions in absorption against the Galactic nonthermal background date back to at least the early 1950s (Scheuer & Ryle 1953), and many surveys of the low-frequency radio sky have detected H II absorption (somewhat more recent examples include Kassim [1988], Dwarakanath & Udaya Shankar [1990], and Braude et al. [1994]). However, the angular resolution of these surveys has always been poor (>30′) due to the limitations of past low-frequency telescopes. Observations with the 74 MHz receiver system on NRAO's Very Large Array (VLA) telescope (e.g., Kassim et al. 1993) now permit much higher resolution imaging. The ~10′ beam used here achieved a compromise between spatial resolution and surface brightness sensitivity to detect many more discrete H II regions than was previously possible. Subarcminute resolution[2] is possible with the system; however, the surface brightness sensitivity is insufficient to detect H II regions on size scales much larger than a few arcminutes. Nevertheless, even near-arcminute resolution is sufficient to establish a direct correspondence between discrete 74 MHz absorption features and many discrete H II regions identified in higher frequency emission surveys.

As is shown in § 3, the high opacity of H II regions at low frequencies causes them to act as an opaque "wall" to incident Galactic background radiation, allowing for the discrimination of radiation originating behind and in front of the H II region. Many such observations along many lines of sight could allow a three-dimensional CR emissivity map to be constructed. Such a map could be of great use in testing CR electron production, diffusion, and aging models (e.g., Longair 1990). Observations at a second frequency would allow for three-dimensional mapping of the spectrum of CR emissivity.

This work is the first step in producing a comprehensive survey of discrete H II absorption with the aim of extracting information about the three-dimensional distribution of the Galactic CR synchrotron emissivity.

2. OBSERVATIONS AND ANALYSIS

Observations presented here were performed with the Naval Research Laboratory (NRL)–NRAO 74/330 MHz system on the VLA in the most compact configurations, which permit the optimal balance between surface brightness sensitivity and resolution for detecting the greatest number of H II absorption features. Four fields were observed (field FWHM ~ 11° at 74 MHz), centered on Galactic (l, b) coordinates of (21.5, −0.9), (11.2, −0.3), (0, 0), and (349.7, +0.2). The Galactic center region ($l,\ b = 0,\ 0$) was observed by the VLA in D configuration on 1999 May 31. The duration of the observation was about 7 hr, with approximately 5.5 hr of on-source time. The 74 and 330 MHz data were taken simultaneously. The 74 MHz bandwidth was 1.5 MHz, which was split into 64 channels in order to facilitate radio frequency interference (RFI) removal and to reduce the effects of bandwidth smearing.[3] Three other pointings were observed cyclically in the DnC hybrid configuration on 2001 September 28–29. The observation was 8 hr in length. However, the first half of the run was lost to especially poor ionospheric weather conditions. Hence, approximately 45 minutes to 1 hr of on-source time per field was obtained.

TABLE 1
74 MHz Observational Summary

(l, b)	Configuration	Date
(349.7, +0.2)	DnC	2001 Sep 28
	C	2001 Aug 28
	B	2001 Mar 1
(0, 0).....................	D	1999 May 31
	C	2001 Sep 5
(11.2, −0.3)..........	DnC	2001 Sep 28
	C	2001 Aug 28
	B	2001 Mar 1
(21.5, −0.5)	DnC	2001 Sep 28
	C	2001 Aug 31

Several of the above fields were previously observed by C. Brogan at 74 MHz with similar compact array configurations. Since there is some u-v overlap in different configurations, these data were included. Table 1 details the observational parameters.

Maps of the Galactic center region at 330 MHz were presented in Nord et al. (2004) and Nord (2005). Data reduction in this work is similar, with a few notable exceptions. Amplitude calibration and bandpass calibration were performed using Cyg A. Due to the paucity of strong point sources at 74 MHz and the large primary beam, standard VLA phase calibration is not practical at 74 MHz. Instead, initial phase calibration was done using Cyg A, these phases were transferred to the field, and then residual phase changes due to ionospheric fluctuations were compensated for with self-calibration. However, this can result in an overall phase shift and hence a positional shift on the sky. For this reason, the first pass of phase self-calibration used a 330 MHz model provided by the data taken simultaneously with the 74 MHz data. As ionospheric refraction effects scale as ν^{-2} (Erickson 1984), the 330 MHz model will suffer much less positional shift and result in much greater astrometric accuracy for the final image. Because only nonthermal sources will be observed in emission at both frequencies, only 330 MHz sources that were known nonthermal emitters were included in the self-calibration model.

RFI excision is a key issue in low-frequency VLA observations. Although algorithms exist that automate the removal of RFI, manual excision is the preferred method, as excision algorithms can miss low-level RFI. First, visibilities with excessive amplitudes (e.g., >100 σ) were flagged. Then the visibility data amplitudes were scrutinized in both Stokes I and V. Stokes V is particularly useful in locating RFI, as there should be very little circular polarization at these frequencies, while RFI is often highly circularly polarized. An additional means by which RFI was localized was the identification of ripples in the image. Determining the spatial frequency of these ripples allowed the offending baseline and time range to be located and removed from the visibility (u-v) data set. See Nord et al. (2004) and Lane et al. (2005) for a more extensive discussion on RFI excision.

After calibration and RFI excision, the data were averaged down to 14 channels. This trade-off slightly increases bandwidth smearing, while significantly reducing the computational cost of imaging. Faceted imaging (Cornwell & Perley 1992) was then employed in order to mitigate noncoplanar effects in the image that are exacerbated by the large fields of view at low frequencies. Approximately 40 facets per field were imaged, and a standard imaging and self-calibration loop was used. Each data set was reduced separately before the data from each field were combined. One final amplitude and phase self-calibration was

[2] A 10″ resolution is possible in the A configuration + Pietown link mode (e.g., Gizani et al. 2005).

[3] After binning, the final frequency channel width was 93.75 kHz. With an ~8′ synthesized beam, bandwidth smearing is an ~1% effect at the edge of the primary beam.

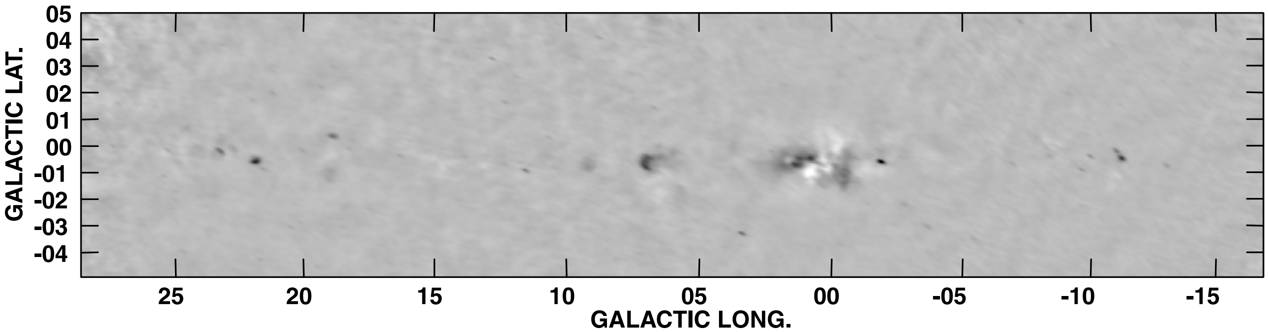

FIG. 1.—The 74 MHz image of the inner Galactic plane. The image has a FWHM resolution of 14.′8 by 6.′2, with a position angle of 8°. The gray scale is linear from −40 to 110 Jy beam^{-1}. Dark regions indicate emission, and white areas are regions of H II region absorption. The image is meant only to orient the reader; measurements were made using data from individual pointings. Due to smoothing, most of the H II regions detected in absorption in this work are not evident in this figure.

performed with a long solution interval in order to resolve any amplitude or phase differences between data sets.

As the fields were observed with differing VLA configurations, have differing *u-v* coverage, and are located at different declinations, the size and shape of the synthesized beam changed between fields. Because roughly equal surface brightness sensitivity is desired in order to compare the different fields, the final images were created using a tapering function in the *u-v* plane. The *u-v* data were weighted by a Gaussian having a 1/*e* point at a *u-v* separation of 700λ ($\sim$2.8 km). The resulting fields have similar resolutions comparable to a C configuration observation but have the surface brightness sensitivity of a D configuration observation.

As the observed fields are spaced approximately one primary beam width from each other, one possible approach for comparing the fields would be to combine all the fields into one image. This approach would have the advantage of greater sensitivity in the regions of overlap. However, as all individual facets are convolved to have the same resolution before being combined, combining all four observed fields results in the final resolution being set by the lowest resolution facet. This is unacceptable, as the increased resolution and surface brightness sensitivity compared to previous low-frequency observations is the main factor permitting the identification of many more individual H II regions. For this reason, all measurements were done on the individual fields. However, for the purpose of examining the entire field imaged, a low-resolution image was created by combining all four fields. The resulting image (Fig. 1) has a FWHM resolution of 14.′8 by 6.′2 with a position angle of 8° and covers a Galactic latitude range of approximately $+5^\circ > b > -5^\circ$ and a Galactic longitude range of $\sim 26^\circ > l > -15^\circ$.

2.1. *Image Sensitivity*

The final rms image sensitivity of a 74 MHz VLA observation is not a simple function of observing time, as it is at higher frequencies. Although not yet fully quantified, the classical confusion limit of a VLA D configuration observation is estimated to be $\approx$0.4 Jy beam^{-1} (A. Cohen 2005, private communication). Furthermore, RFI and an incomplete understanding of ionospheric effects can introduce distorted data, resulting in a situation in which more data may actually adversely affect image quality. Good *u-v* coverage and a calm ionosphere and RFI environment are more important than observation length. The images created in the course of this work are approaching as low a noise level as the present VLA 74 MHz system will allow while maintaining the surface brightness sensitivity required to detect diffuse H II regions. The addition of B and A configuration data could well decrease the confusion limit, but higher order ionospheric effects become very difficult to overcome in these configurations. Further work in the detection and quantification of H II regions in absorption at low frequencies will likely have to await the high surface brightness sensitivity, high-resolution, fully ionospherically compensated images expected out of the next generation of low-frequency radio telescopes such as the Long Wavelength Array (LWA) and the Low Frequency Array.

3. H II ABSORPTION REGION INTERPRETATION

Following Kassim (1987), a single-dish radio telescope observing an H II region with an angular extent larger than the primary beam of the telescope would observe a brightness temperature (in kelvins) of

$$T_h = T_e(1 - e^{-\tau}) + T_{\rm gb}e^{-\tau} + T_{\rm gf},$$

where T_e is the electron temperature of the H II region, $T_{\rm gb}$ is the brightness temperature of the CR electron nonthermal emission behind the H II region, $T_{\rm gf}$ is the brightness temperature of the CR electron nonthermal emission between the H II region and the observer, and τ is the optical depth of the H II region (any extragalactic contribution is assumed to be negligible). For a typical Galactic H II region,[4] $\tau_{74\,\rm MHz} \gg 1$, reducing the above equation to

$$T_h = T_e + T_{\rm gf}.$$

The single dish measuring a line of sight near the H II region would measure

$$T_{\rm gt} = T_{\rm gf} + T_{\rm gb},$$

where $T_{\rm gt}$ is brightness temperature from the Galactic total CR electron synchrotron emission. As an interferometer is insensitive to the total flux, it measures the difference between these two, giving an observed brightness temperature of the H II region of

$$T_{\rm obs} = (T_e + T_{\rm gf}) - (T_{\rm gf} + T_{\rm gb}) = T_e - T_{\rm gb}.$$

[4] Here $\tau(\nu) \sim 8.2 \times 10^{-2} T_e^{-1.35} \nu^{-2.1}$ times the emission measure (EM) for T_e in K, ν in GHz, and EM in pc cm^{-6} (Harwit 1998). For a typical $T_e \sim 7000$ K and EM $\sim 10^5$ pc cm^{-6}, $\tau \sim 12.5$ at $\nu = 74$ MHz.

TABLE 2

H II Regions in the Field of G21.5−0.5

Catalog No. (1)	l (2)	b (3)	R.A. (4)	Decl. (5)	I (Jy beam^{-1}) (6)	T_{obs} ($\times 10^3$ K) (7)	T_{gb} ($\times 10^3$ K) (8)	T_e ($\times 10^3$ K) (9)	D (kpc) (10)	ε (K pc^{-1}) (11)
201	15.1	−0.7	18 20 37.5	−16 08 51	−4.1 ± 1.3	−7.3 ± 2.3	13.2 ± 2.5	5.9 ± 1.0	2.1	0.51 ± 0.10
204	15.2	−0.6	18 20 27.2	−16 00 43	−4.4 ± 1.3	−8.0 ± 2.3	17.5 ± 2.5	9.5 ± 1.0	1.8	0.66 ± 0.09
218	16.9	+0.8	18 18 40.1	−13 51 09	−3.9 ± 0.9	−6.9 ± 1.7	13.0 ± 1.9	6.1 ± 1.0	2.7	0.52 ± 0.08
219	17.0	+0.8	18 18 51.8	−13 45 52	−3.9 ± 0.9	−7.0 ± 1.6	13.1 ± 1.9	6.1 ± 1.0	2.5	0.52 ± 0.08
220	17.0	+0.9	18 18 30.1	−13 43 01	−5.6 ± 0.9	−10.0 ± 1.6	18.1 ± 1.9	8.1 ± 1.0	2.7	0.72 ± 0.08
224	17.1	+0.8	18 19 03.5	−13 40 34	−5.4 ± 0.9	−9.7 ± 1.6	16.7[a] ± 2.6	7.0 ± 2.0	...	...
234	18.2	+1.9	18 17 13.1	−12 11 13	−2.4 ± 0.8	−4.3 ± 1.5	10.1 ± 1.8	5.8 ± 1.0	...	...
236	18.3	−0.3	18 25 22.2	−13 08 02	−2.3 ± 0.7	−4.2 ± 1.3	9.5 ± 1.6	5.3 ± 1.0	4.0	0.40 ± 0.07
237	18.3	+1.2	18 19 56.2	−12 25 47	−3.2 ± 0.8	−5.8 ± 1.4	12.8[a] ± 2.4	7.0 ± 2.0	...	...
238	18.3	+1.9	18 17 24.7	−12 05 56	−3.1 ± 0.8	−5.6 ± 1.5	11.4 ± 1.8	5.8 ± 1.0	2.8	0.46 ± 0.07
241	18.5	+1.9	18 17 47.9	−11 55 22	−3.5 ± 0.9	−6.3 ± 1.7	13.3[a] ± 2.6	7.0 ± 2.0	...	...
242	18.5	+2.0	18 17 26.3	−11 52 32	−2.7 ± 0.8	−4.8 ± 1.5	11.8[a] ± 2.5	7.0 ± 2.0	...	...
244	18.6	+1.9	18 17 59.5	−11 50 05	−3.5 ± 0.8	−6.3 ± 1.4	13.3[a] ± 2.5	7.0 ± 2.0	...	...
245	18.7	+2.0	18 17 49.5	−11 41 58	−3.3 ± 0.8	−6.0 ± 1.5	13.0[a] ± 2.5	7.0 ± 2.0	2.5	0.51 ± 0.10
246	18.8	+1.8	18 18 44.3	−11 42 21	−3.6 ± 0.8	−6.5 ± 1.4	13.5[a] ± 2.4	7.0 ± 2.0	...	...
248	18.9	−0.5	18 27 14.6	−12 41 46	−2.1 ± 0.7	−3.8 ± 1.2	9.7 ± 1.6	5.9 ± 1.0	4.6	0.42 ± 0.07
249	18.9	−0.4	18 26 52.8	−12 38 59	−5.1 ± 0.7	−9.2 ± 1.2	14.7 ± 1.6	5.5 ± 1.0	4.7	0.63 ± 0.07
251	19.0	−0.4	18 27 04.3	−12 33 40	−5.2 ± 0.7	−9.3 ± 1.2	16.3[a] ± 2.3	7.0 ± 2.0	...	...
252	19.0	−0.3	18 26 42.5	−12 30 52	−2.8 ± 0.7	−5.1 ± 1.2	10.3 ± 1.6	5.2 ± 1.0	...	...
253	19.0	−0.0	18 25 37.3	−12 22 29	−1.9 ± 0.7	−3.3 ± 1.2	8.5 ± 1.6	5.2 ± 1.0	3.8	0.35 ± 0.07
254	19.1	−0.3	18 26 54.0	−12 25 34	−3.5 ± 0.7	−6.3 ± 1.2	10.4 ± 1.6	4.1 ± 1.0	4.6	0.45 ± 0.07
266	20.2	−0.9	18 31 09.7	−11 43 49	−1.7 ± 0.6	−3.1 ± 1.1	10.1[a] ± 2.3	7.0 ± 2.0	...	...
267	20.3	−0.9	18 31 21.1	−11 38 30	−2.0 ± 0.6	−3.6 ± 1.1	10.6[a] ± 2.3	7.0 ± 2.0	12.3	0.69 ± 0.15
268	20.3	−0.8	18 30 59.3	−11 35 43	−2.4 ± 0.6	−4.2 ± 1.1	11.2[a] ± 2.3	7.0 ± 2.0	...	...
286	22.9	−0.3	18 34 04.0	−09 03 30	−2.9 ± 0.6	−5.2 ± 1.1	10.3 ± 1.5	5.1 ± 1.0	11.1	0.62 ± 0.09
288	23.0	−0.4	18 34 36.8	−09 00 57	−2.2 ± 0.6	−4.0 ± 1.1	11.8 ± 1.5	7.8 ± 1.0	10.9	0.71 ± 0.09
309	24.2	+0.2	18 34 41.7	−07 40 27	−2.3 ± 0.7	−4.1 ± 1.3	11.1[a] ± 2.4	7.0 ± 2.0	9.3	0.61 ± 0.13
311	24.4	+0.1	18 35 25.5	−07 32 34	−2.9 ± 0.7	−5.1 ± 1.3	10.6 ± 1.6	5.5 ± 1.0	6.2	0.50 ± 0.08
314	24.5	+0.2	18 35 15.1	−07 24 28	−3.4 ± 0.7	−6.1 ± 1.3	10.8 ± 1.7	4.7 ± 1.0	6.5	0.51 ± 0.08
316	24.6	−0.2	18 36 52.2	−07 30 11	−4.0 ± 0.7	−7.2 ± 1.3	14.2[a] ± 2.4	7.0 ± 2.0	...	...
319	24.7	−0.2	18 37 03.4	−07 24 51	−4.7 ± 0.7	−8.4 ± 1.3	14.1 ± 1.7	5.7 ± 1.0	10.3	0.82 ± 0.10
321	24.7	−0.1	18 36 41.9	−07 22 06	−3.4 ± 0.7	−6.2 ± 1.3	13.2[a] ± 2.4	7.0 ± 2.0	6.2	0.62 ± 0.11
322	24.8	+0.1	18 36 10.0	−07 11 15	−5.4 ± 0.8	−9.8 ± 1.4	14.7 ± 1.7	5.0 ± 1.0	6.1	0.69 ± 0.08
325	25.3	−0.3	18 38 31.5	−06 55 38	−4.2 ± 0.8	−7.6 ± 1.5	13.3 ± 1.8	5.7 ± 1.0	11.2	0.82 ± 0.11
327	25.4	−0.3	18 38 42.6	−06 50 18	−4.5 ± 0.8	−8.0 ± 1.5	16.1 ± 1.8	8.1 ± 1.0	11.2	1.00 ± 0.11
328	25.4	−0.2	18 38 21.1	−06 47 33	−4.6 ± 0.8	−8.3 ± 1.5	14.3 ± 1.8	6.0 ± 1.0	11.4	0.90 ± 0.11

Notes.—Tables 2–5 detail the H II regions detected in absorption from § 4. Col. (1): Catalog number from Paladini et al. (2003). Col. (2): Galactic longitude (l) in degrees. Col. (3): Galactic latitude (b) in degrees. Cols. (4) and (5): Right ascension and declination (J2000.0); units of right ascension are hours, minutes, and seconds, and units of declination are degrees, arcminutes, and arcseconds. Col. (6): Observed intensity in janskys per beam. Col. (7): Sky brightness temperature derived from the measured intensity. Col. (8): Integrated cosmic-ray electron brightness temperature of the column behind the H II region. Col. (9): Electron temperature of the H II region ($\times 10^3$ K). Col. (10): Distance from the Sun to the H II region (in kiloparsecs, when known). Col. (11): Emissivity (in K pc^{-1}) of the column behind the H II region using the assumptions of § 5. The field is centered on $18^h33^m36^s.4$, $-10°46'38''.8$ (J2000.0). The resolution element is $7'.33 \times 4'.75$, and the position angle is 12° (1 Jy beam^{-1} = 1790 K). The rms at the center of the field is 0.6 Jy beam^{-1}.

[a] The electron temperature of this H II region was unavailable, so a value of 7000 ± 2000 K was used in the calculation of the background brightness temperature.

For typical electron and Galactic background temperatures ($T_e \approx 7000$ K and $T_{gb} \approx 20{,}000$ K near the Galactic center), we expect the observed T_{obs} to be negative.

If the electron temperature of the H II region is either known from higher frequency measurements or can be estimated, the brightness temperature of the column *behind* the H II region is then directly calculated. If an appropriate measure of the total emission (T_{gt}) exists, the brightness temperature of the column between the H II region and the observer may be derived. When the path length (D) over which the brightness temperature is integrated is known or can be deduced from reasonable physical assumptions, the emissivity may then be calculated ($\varepsilon = T/D$ K pc^{-1}). This ability to split the total line-of-sight emission into columns behind and in front of the H II region allows information concerning the *three-dimensional* distribution of Galactic CR emissivity to be extracted. This technique is unique to the low-frequency radio regime.

4. A CATALOG OF H II REGIONS DETECTED IN ABSORPTION

After the calibration and imaging described in § 2 were completed, the four fields were scrutinized for regions of negative intensity. However, negative regions in an interferometer map can be image artifacts due to overcleaning, incomplete *u-v* coverage, small errors in self-calibration, or other factors. For this reason, an a priori search was used to search for H II absorption features. We used the catalog of Paladini et al. (2003), which is a compilation of many separate H II region catalogs from higher frequency observations, for the identification. Compact H II regions (smaller than 1′.5) were excluded, as they would be undetectable

TABLE 3
H II Regions in the Field of G11.2−0.3

Catalog No. (1)	l (2)	b (3)	R.A. (4)	Decl. (5)	I (Jy beam^{-1}) (6)	T_{obs} ($\times10^3$ K) (7)	T_{gb} ($\times10^3$ K) (8)	T_e ($\times10^3$ K) (9)	D (kpc) (10)	ε (K pc^{-1}) (11)
66	6	−1.3	18 04 13	−24 24 59	−3.9 ± 1.191	−6.4 ± 2.0	13.4[a] ± 2.8	7.0 ± 2.0	...	...
67	6	−1.2	18 03 50	−24 22 02	−4.5 ± 1.187	−7.4 ± 2.0	14.4[a] ± 2.8	7.0 ± 2.0	...	...
69	6.1	−0.6	18 01 45.7	−23 59 05	−4.0 ± 1.146	−6.7 ± 1.9	13.7[a] ± 2.8	7.0 ± 2.0	12.7	0.87 ± 0.17
71	6.2	−1.2	18 04 15.9	−24 11 35	−4.8 ± 1.138	−8.0 ± 1.9	15.0[a] ± 2.7	7.0 ± 2.0	...	...
72	6.2	−0.6	18 01 58.6	−23 53 52	−3.9 ± 1.122	−6.4 ± 1.9	13.4[a] ± 2.7	7.0 ± 2.0	12.9	0.87 ± 0.18
108	8	−0.2	18 04 19	−22 08 03	−2.8 ± 0.842	−4.6 ± 1.4	11.6[a] ± 2.4	7.0 ± 2.0	11.8	0.70 ± 0.15
163	12.7	−0.2	18 14 00.9	−18 01 20	−5.7 ± 0.729	−9.4 ± 1.2	13.9 ± 1.6	4.5 ± 1.0	4.8	0.59 ± 0.07
165	12.8	−0.2	18 14 13	−17 56 04	−5.6 ± 0.733	−9.3 ± 1.2	15.3 ± 1.6	6.0 ± 1.0	3.8	0.63 ± 0.06
166	12.8	+0.4	18 12 00.3	−17 38 49	−2.7 ± 0.741	−4.5 ± 1.2	11.5[a] ± 2.3	7.0 ± 2.0	13.9	0.81 ± 0.16
168	12.9	−0.2	18 14 25	−17 50 48	−3.7 ± 0.738	−6.0 ± 1.2	12.1 ± 1.6	6.1 ± 1.0	3.7	0.49 ± 0.06
177	13.9	−0.1	18 16 02.9	−16 55 12	−2.9 ± 0.800	−4.8 ± 1.3	11.8[a] ± 2.4	7.0 ± 2.0	...	...
178	13.9	−0	18 15 40.8	−16 52 21	−3.5 ± 0.800	−5.8 ± 1.3	12.8[a] ± 2.4	7.0 ± 2.0	13.1	0.85 ± 0.16
181	14	−0.1	18 16 14.8	−16 49 56	−4.3 ± 0.808	−7.0 ± 1.3	12.6 ± 1.7	5.5 ± 1.0	3.6	0.51 ± 0.07
184	14.2	−0.3	18 17 22.8	−16 45 04	−3.5 ± 0.825	−5.8 ± 1.4	12.8[a] ± 2.4	7.0 ± 2.0	...	...
185	14.2	−0.2	18 17 00.7	−16 42 13	−2.7 ± 0.825	−4.4 ± 1.4	11.4[a] ± 2.4	7.0 ± 2.0	3.7	0.47 ± 0.10
186	14.2	−0.1	18 16 38.7	−16 39 22	−3.4 ± 0.826	−5.6 ± 1.4	12.6[a] ± 2.4	7.0 ± 2.0	...	...
187	14.3	−0.2	18 17 12.6	−16 36 57	−6.9 ± 0.835	−11.4 ± 1.4	18.4[a] ± 2.4	7.0 ± 2.0	...	...
190	14.4	−0.6	18 18 52.7	−16 43 02	−2.8 ± 0.845	−4.6 ± 1.4	11.6[a] ± 2.4	7.0 ± 2.0	...	...
191	14.4	−0.1	18 17 02.5	−16 28 49	−5.4 ± 0.845	−9.0 ± 1.4	16.0[a] ± 2.4	7.0 ± 2.0	12.7	1.04 ± 0.16
192	14.5	−0.6	18 19 04.6	−16 37 45	−4.0 ± 0.855	−6.6 ± 1.4	13.6[a] ± 2.4	7.0 ± 2.0	...	...
195	14.6	+0.1	18 16 42.2	−16 12 33	−4.9 ± 0.869	−8.1 ± 1.4	13.4 ± 1.7	5.3 ± 1.0	...	...
218	16.9	+0.8	18 18 40.1	−13 51 09	−5.6 ± 1.356	−9.2 ± 2.2	15.3 ± 2.5	6.1 ± 1.0	2.7	0.60 ± 0.10

Notes.—Tables 2–5 detail the H II regions detected in absorption from § 4. Col. (1): Catalog number from Paladini et al. (2003). Col. (2): Galactic longitude (l) in degrees. Col. (3): Galactic latitude (b) in degrees. Cols. (4) and (5): Right ascension and declination (J2000.0); units of right ascension are hours, minutes, and seconds, and units of declination are degrees, arcminutes, and arcseconds. Col. (6): Observed intensity in janskys per beam. Col. (7): Sky brightness temperature derived from the measured intensity. Col. (8): Integrated cosmic-ray electron brightness temperature of the column behind the H II region. Col. (9): Electron temperature of the H II region ($\times10^3$ K). Col. (10): Distance from the Sun to the H II region (in kiloparsecs, when known). Col. (11): Emissivity (in K pc^{-1}) of the column behind the H II region using the assumptions of § 5. The field is centered on $18^h11^m30^s.600$, $-19°25'16''.000$ (J2000.0). The resolution element is $6'.67 \times 5'.67$, and the position angle is $-10°$ (1 Jy beam^{-1} = 1650 K). The rms at the center of the field is 0.7 Jy beam^{-1}.

[a] The electron temperature of this H II region was unavailable, so a value of 7000 ± 2000 K was used in the calculation of the background brightness temperature.

due to beam dilution, and the remaining H II regions were overlaid on the imaged regions. Any known H II region that was coincident with an intensity $\leq -3\ \sigma$ was considered a detection. The image intensity at the location of the H II region was then used to derive a sky brightness temperature.[5] Tables 2–5 detail the 92 absorption features that are detected. No significant regions ($\geq$3 contiguous beam areas) of negative intensity that did not coincide with a known H II region were found, indicating that these absorption features are all astrophysical in origin[6] and not image artifacts. Furthermore, the image median far from emission or absorption regions was measured to be near zero, confirming the assumption that the interferometer is not sensitive to the large-scale emission. A representative image of an H II absorption feature is shown in Figure 2.

4.1. *Nondetections and Detection Bias*

Nearly 300 H II regions (of size $\geq 1'.5$) in the Paladini et al. (2003) catalog and within the area imaged were not detected. As H II absorption features are not detected via their own emission but through the emission they are blocking, the sensitivity in detecting them depends on the temperature of the column behind them. This is a particularly vexing detection bias, as it not only varies as a function of Galactic longitude, Galactic latitude, and distance, but the temperature of the background column is precisely the quantity in which we are interested, i.e., a model compensating for detection biases is the very model we are trying to create with the observations. In this case and in cases in which a large amount of the data in a given sample is contained in nondetections, the statistical techniques of survival (regression) analysis are of use (e.g., Isobe et al. 1986). These techniques attempt to not only fit the measured data but also extract information pertaining to the underlying distribution by assuming a functional form for the nondetection residuals and fitting this well. In order to perform this analysis, nondetection upper limits must be measured. The 3 σ upper limits on the background temperature of the 134 H II regions in the field with known distances that were not detected are detailed in Table 6.

5. DERIVING COSMIC-RAY EMISSIVITY BEHIND THE H II REGIONS

From § 3, the quantity directly measured from the images is $T_{obs} = T_e - T_{gb}$. With knowledge of the electron temperatures of the H II regions or, lacking that, adopting an assumed value (7000 K; see below), the integrated brightness temperature of the column behind the H II region can be derived. Coupled with the distance to the H II region (when known), this gives many pencil-beam integrated brightness temperatures with which to reconstruct the three-dimensional CR electron emissivity distribution. Note that this measurement is independent of assumptions of Galactic structure, a feature unique to this method.

Electron temperatures are either known from higher frequency studies (Paladini et al. 2004 and references therein) or can be estimated. A value of 7000 ± 2000 K was used as an estimate for

[5] Here $I = 2kT\Omega/\lambda^2$, where I is the image intensity in W m^{-2} Hz^{-1} sr^{-1}, k is Boltzmann's constant, λ is the wavelength, and Ω is the solid angle of the beam.

[6] With 92 sources at 3 σ confidence, one would expect less than one spurious detection.

TABLE 4

H II Regions in the Field of the Galactic Center

Catalog No. (1)	l (2)	b (3)	R.A. (4)	Decl. (5)	I (Jy beam^{-1}) (6)	T_{obs} ($\times10^3$ K) (7)	T_{gb} ($\times10^3$ K) (8)	T_e ($\times10^3$ K) (9)	D (kpc) (10)	ε (K pc^{-1}) (11)
1	0.1	+0	17 45 51.3	−28 51 08	−7.7 ± 0.8	−4.1 ± 0.4	11.1[a] ± 2.0	7.0 ± 2.0	...	...
4	0.3	−0.5	17 48 17	−28 56 25	−34.1 ± 0.8	−18.3 ± 0.4	25.3[a] ± 2.0	7.0 ± 2.0	...	...
5	0.4	−0.8	17 49 41.7	−29 00 33	−17.1 ± 0.8	−9.2 ± 0.4	16.2[a] ± 2.0	7.0 ± 2.0	...	...
6	0.4	−0.5	17 48 31.1	−28 51 17	−43.4 ± 0.8	−23.3 ± 0.4	30.8 ± 1.1	7.5 ± 1.0	...	...
7	0.5	−0.7	17 49 32.2	−28 52 19	−21.0 ± 0.8	−11.3 ± 0.4	16.8 ± 1.1	5.5 ± 1.0	...	...
10	0.6	−0.9	17 50 33.3	−28 53 19	−8.8 ± 0.8	−4.7 ± 0.4	11.7[a] ± 2.0	7.0 ± 2.0	...	...
11	0.6	−0.6	17 49 22.8	−28 44 05	−28.7 ± 0.8	−15.4 ± 0.4	22.4[a] ± 2.0	7.0 ± 2.0	...	...
12	0.6	−0.5	17 48 59.3	−28 41 00	−45.7 ± 0.8	−24.6 ± 0.4	38.1 ± 1.1	13.5 ± 1.0	...	...
13	0.6	−0.4	17 48 35.9	−28 37 54	−45.4 ± 0.8	−24.4 ± 0.4	29.6 ± 1.1	5.2 ± 1.0	...	...
22	2.3	+1.4	17 45 37.8	−26 14 42	−5.5 ± 0.9	−3.0 ± 0.5	10.0[a] ± 2.1	7.0 ± 2.0	...	...
26	2.4	+1.4	17 45 51.8	−26 09 35	−6.8 ± 0.9	−3.6 ± 0.5	10.6[a] ± 2.1	7.0 ± 2.0	...	...
30	3.3	+0	17 53 16.4	−26 06 26	−4.0 ± 1.0	−2.1 ± 0.5	9.1[a] ± 2.1	7.0 ± 2.0	...	...
65	5.9	−0.4	18 00 34	−24 03 34	−12.1 ± 1.6	−6.5 ± 0.9	13.2 ± 1.3	6.7 ± 1.0	...	...
66	6	−1.3	18 04 13	−24 24 59	−12.3 ± 1.7	−6.6 ± 0.9	13.6[a] ± 2.2	7.0 ± 2.0	...	...
67	6	−1.2	18 03 50	−24 22 02	−19.0 ± 1.7	−10.2 ± 0.9	17.2[a] ± 2.2	7.0 ± 2.0	...	...
69	6.1	−0.6	18 01 45.7	−23 59 05	−13.3 ± 1.7	−7.2 ± 0.9	14.2[a] ± 2.2	7.0 ± 2.0	12.7	0.90 ± 0.14
71	6.2	−1.2	18 04 15.9	−24 11 35	−20.1 ± 1.8	−10.8 ± 1.0	17.8[a] ± 2.2	7.0 ± 2.0	...	...
72	6.2	−0.6	18 01 58.6	−23 53 52	−14.9 ± 1.7	−8.0 ± 0.9	15.0[a] ± 2.2	7.0 ± 2.0	12.9	0.97 ± 0.14
75	6.4	−0.5	18 02 01.7	−23 40 28	−6.8 ± 1.8	−3.6 ± 1.0	10.6[a] ± 2.2	7.0 ± 2.0	3.8	0.43 ± 0.09
78	6.5	−1.4	18 05 40.3	−24 01 46	−8.2 ± 2.0	−4.4 ± 1.1	11.4[a] ± 2.3	7.0 ± 2.0	...	...
109	8.1	+0.2	18 03 01.6	−21 51 01	−15.8 ± 3.3	−8.5 ± 1.8	15.0 ± 2.0	6.5 ± 1.0	3.5	0.60 ± 0.08
1401	353.1	+0.6	17 25 43.2	−34 25 19	−11.2 ± 2.1	−6.0 ± 1.1	13.0[a] ± 2.3	7.0 ± 2.0	...	...
1402	353.1	+0.7	17 25 19.1	−34 21 57	−13.0 ± 2.1	−7.0 ± 1.1	14.0[a] ± 2.3	7.0 ± 2.0	...	...
1403	353.2	+0.7	17 25 35.4	−34 16 59	−20.5 ± 2.0	−11.0 ± 1.1	18.0[a] ± 2.3	7.0 ± 2.0	...	...
1404	353.2	+0.9	17 24 47.3	−34 10 15	−23.3 ± 2.1	−12.5 ± 1.1	19.5[a] ± 2.3	7.0 ± 2.0	...	...
1407	353.4	+0.5	17 26 56	−34 13 44	−17.5 ± 1.9	−9.4 ± 1.0	16.4[a] ± 2.2	7.0 ± 2.0	...	...
1428	357.5	−1.4	17 45 06.9	−31 48 02	−3.6 ± 0.9	−2.0 ± 0.5	9.0[a] ± 2.1	7.0 ± 2.0	...	...
1429	358	−0.2	17 41 33.8	−30 44 42	−5.1 ± 0.9	−2.8 ± 0.5	9.8[a] ± 2.1	7.0 ± 2.0	...	...
1431	358.6	−0.1	17 42 38.3	−30 10 57	−3.3 ± 0.8	−1.8 ± 0.4	8.8[a] ± 2.0	7.0 ± 2.0	...	...
1440	359.7	−0.4	17 46 28.1	−29 24 06	−3.1 ± 0.8	−1.7 ± 0.4	10.3 ± 2.0	8.6 ± 1.0	...	...
1441	359.9	−0.1	17 45 46.2	−29 04 30	−14.1 ± 0.8	−7.6 ± 0.4	13.6 ± 2.0	6.0 ± 1.0	...	...
1442	359.9	−0	17 45 22.8	−29 01 22	−20.4 ± 0.8	−11.0 ± 0.4	18.0[a] ± 2.0	7.0 ± 2.0	...	...

Notes.—Tables 2–5 detail the H II regions detected in absorption from § 4. Col. (1): Catalog number from Paladini et al. (2003). Col. (2): Galactic longitude (l) in degrees. Col. (3): Galactic latitude (b) in degrees. Cols. (4) and (5): Right ascension and declination (J2000.0); units of right ascension are hours, minutes, and seconds, and units of declination are degrees, arcminutes, and arcseconds. Col. (6): Observed intensity in janskys per beam. Col. (7): Sky brightness temperature derived from the measured intensity. Col. (8): Integrated cosmic-ray electron brightness temperature of the column behind the H II region. Col. (9): Electron temperature of the H II region ($\times10^3$ K). Col. (10): Distance from the Sun to the H II region (in kiloparsecs, when known). Col. (11): Emissivity (in K pc^{-1}) of the column behind the H II region using the assumptions of § 5. The field is centered on $17^h45^m40\overset{s}{.}0$, $-29°00'27\overset{''}{.}9$ (J2000.0). The resolution element is $17\overset{'}{.}41 \times 6\overset{'}{.}67$, and the position angle is 5° (1 Jy beam^{-1} = 537 K). The rms at the center of the field is 0.8 Jy beam^{-1}.

[a] The electron temperature of this H II region was unavailable, so a value of 7000 ± 2000 K was used in the calculation of the background brightness temperature.

TABLE 5

H II Regions in the Field of G349.7+0.2

Catalog No. (1)	l (2)	b (3)	R.A. (4)	Decl. (5)	I (Jy beam^{-1}) (6)	T_{obs} ($\times10^3$ K) (7)	T_{gb} ($\times10^3$ K) (8)	T_e ($\times10^3$ K) (9)	D (kpc) (10)	ε (K pc^{-1}) (11)
1353	348.6	−0.6	17 17 53.5	−38 48 24	−5.5 ± 0.6	−8.2 ± 0.9	13.0 ± 1.4	4.8 ± 1.0	2.7	0.51 ± 0.05
1354	348.7	−1	17 19 52.2	−38 57 17	−2.2 ± 0.6	−3.3 ± 0.9	9.5 ± 1.4	6.2 ± 1.0	2.0	0.36 ± 0.05
1375	351	+0.7	17 19 29.2	−36 05 44	−4.6 ± 0.6	−6.8 ± 0.9	13.8[a] ± 2.2	7 ± 2.0	...	...
1376	351.2	+0.5	17 20 51.9	−36 02 45	−4.4 ± 0.6	−6.7 ± 0.9	13.7[a] ± 2.2	7 ± 2.0	...	...
1379	351.4	+0.7	17 20 37.1	−35 46 03	−4.2 ± 0.6	−6.2 ± 0.9	12.3 ± 1.4	6.1 ± 1.0	...	...
1380	351.5	−0.5	17 25 47.7	−36 21 49	−2.1 ± 0.6	−3.2 ± 1.0	8.9 ± 1.4	5.7 ± 1.0	3.3	0.36 ± 0.06
1411	354.2	−0.1	17 31 28.9	−33 53 39	−3.3 ± 0.9	−4.9 ± 1.3	10.2 ± 1.6	5.3 ± 1.0	5.1	0.44 ± 0.07
1412	354.2	−0	17 31 04.8	−33 50 21	−2.9 ± 0.9	−4.3 ± 1.3	9.6 ± 1.6	5.3 ± 1.0	...	...

Notes.—Tables 2–5 detail the H II regions detected in absorption from § 4. Col. (1): Catalog number from Paladini et al. (2003). Col. (2): Galactic longitude (l) in degrees. Col. (3): Galactic latitude (b) in degrees. Cols. (4) and (5): Right ascension and declination (J2000.0); units of right ascension are hours, minutes, and seconds, and units of declination are degrees, arcminutes, and arcseconds. Col. (6): Observed intensity in janskys per beam. Col. (7): Sky brightness temperature derived from the measured intensity. Col. (8): Integrated cosmic-ray electron brightness temperature of the column behind the H II region. Col. (9): Electron temperature of the H II region ($\times10^3$ K). Col. (10): Distance from the Sun to the H II region (in kiloparsecs, when known). Col. (11): Emissivity (in K pc^{-1}) of the column behind the H II region using the assumptions of § 5. The field is centered on $17^h18^m02\overset{s}{.}700$, $-37°26'13\overset{''}{.}0$ (J2000.0). The resolution element is $8\overset{'}{.}33 \times 5\overset{'}{.}00$, and the position angle is 10° (1 Jy beam^{-1} = 1490 K). The rms at the center of the field is 0.6 Jy beam^{-1}.

[a] The electron temperature of this H II region was unavailable, so a value of 7000 ± 2000 K was used in the calculation of the background brightness temperature.

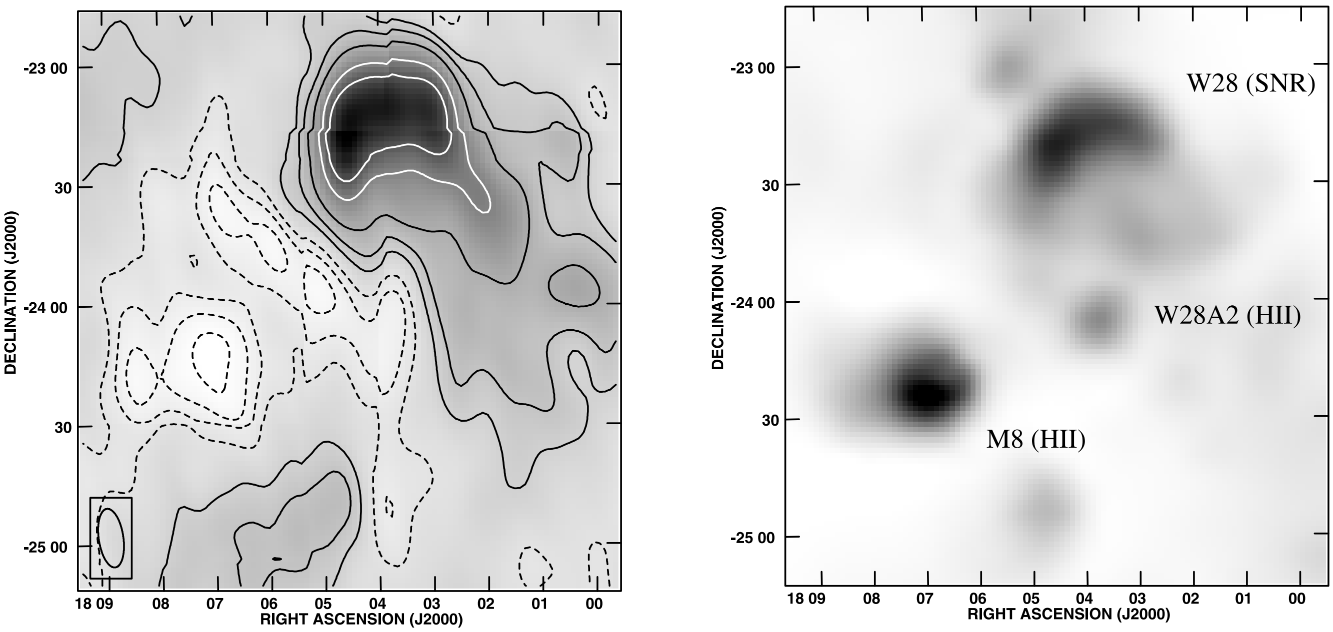

FIG. 2.—*Left:* Region around the H II region M8 at 74 MHz. Contours are −8, −4, −2, 2, 5, 10, 20, and 30 times the local rms of 1.4 Jy beam^{-1} (750 K). Dashed contours indicate regions of negative intensity. The gray scale is linear between −12 and 70 Jy beam^{-1}, with dark areas indicating areas of emission and white areas indicating areas of absorption, and the image is centered on $l = 6°$, $b = -1.°1$. *Right:* Same region from the 1.4 GHz Bonn single-dish survey (Reich et al. 1990). Note that the nearby SNR W28 (G6.67−0.42, *upper right*) is seen in emission in both frames, but the H II regions M8 and W28A-2 are seen in emission at 1.4 GHz and seen in absorption at 74 MHz. This is illustrative of the nonthermal nature of the SNR emission and the thermal absorption due to the H II regions.

the unknown electron temperatures based on the studies of Paladini et al. (2004). The trend for H II regions to have higher electron temperatures with increasing galactocentric radius (e.g., Paladini et al. 2004, Fig. 4) is not explicitly taken into account. However, the correlation is a weak one, and the narrow range of radii in this sample (∼3–8 kpc) puts any systematic variation well within the error bars. Thus, for all H II regions detected in absorption an integrated brightness temperature of the column behind the H II region is derived; for nondetections, an upper limit is derived. These values are detailed in Tables 2–5 and in Table 6.

For many of the H II regions in the survey area, kinematic distances have been determined by Paladini et al. (2004 and references therein), who used absorption-line data and a correlation between luminosity and linear diameter to resolve distance ambiguities when present. Knowledge of the path length of the column behind the H II region along with the measured integrated brightness temperature allows for the average emissivity of the column behind the H II region to be derived ($\varepsilon = T/D$ K pc^{-1}). For the moment, we model the Galactic CR disk as an axisymmetric cylinder having a radius of 20 kpc and a vertical height of 1 kpc above and below the plane (Ferrière 2001 and references therein), and the Earth is assumed to be 8.5 kpc from the Galactic center (IAU 1985 standard). As all detected absorption features are $\leq 1.°3$ from the Galactic plane, all background lines of sight traverse the entire Galactic CR disk (i.e., no lines of sight exit the top or bottom of the disk), and therefore, the disk can be treated two-dimensionally. The emissivities derived are listed in Tables 2–5. Figure 3 graphically shows the lines of sight along which emissivities are measured.

As a check, we compare our emissivity values with values derived from other methods. Modeling of Galactic CR emissivity by Beuermann et al. (1985) based on the all-sky 408 MHz single-dish maps of Haslam et al. (1982) derive a typical CR emissivity of ∼10 K kpc^{-1} at 408 MHz. Platania et al. (2003) examine the temperature spectral index of Galactic nonthermal emission through a comparison of the Haslam et al. (1982) 408 MHz map and the 1400 MHz map of Reich (1982) and arrive at $T(\nu) \propto \nu^{-2.7}$. With these values, the expected emissivity at 74 MHz may be estimated. Scaling from 408 MHz, a value of ∼1 K pc^{-1} is expected at 74 MHz. The emissivity values measured in this work agree remarkably well with this estimate, with values in the range 0.35 K pc^{-1} $< \varepsilon <$ 1.0 K pc^{-1}.

TABLE 6

H II REGION NONDETECTIONS

Catalog No. (1)	l (2)	b (3)	D (kpc) (4)	T_e ($\times 10^3$ K) (5)	T_{gb} ($\times 10^3$ K) (6)
43	4.6	−0.1	12.3	3.6	5.4
48	5	+0.3	13.6	. . .	8.9
60	5.5	−0.2	4.8	6.4	7.3
80	6.5	+0.1	3.1	7.5	17.2
81	6.6	−0.3	3.4	5.8	16.6
82	6.6	−0.1	3.0	6.7	22.5
86	6.7	−0.2	3.7	8.1	36.5
93	7	−0.2	3.0	7.4	28.0
100	7.4	+0.7	13.1	4.7	8.7
112	8.3	−0.1	11.6	. . .	9.8

NOTES.—Col. (1): Catalog number from Paladini et al. (2003). Col. (2): Galactic longitude (l) in degrees. Col. (3): Galactic latitude (b) in degrees. Col. (4): Geocentric distance (in kiloparsecs). Col. (5): Electron temperature ($\times 10^3$ K, when available). Col. (6): 3 σ nondetection upper limit of the integrated cosmic-ray electron brightness temperature of the column behind the H II region ($\times 10^3$ K; 7000 K used for electron temperature when not available). Table 6 is published in its entirety in the electronic edition of the *Astronomical Journal*. A portion is shown here for guidance regarding its form and content.

6. GALACTIC COSMIC-RAY EMISSIVITY MODELING

The 42 emissivity path lengths (and 134 upper limits) measured in this work can form the starting point from which one can attempt to model the three-dimensional Galactic CR emissivity.

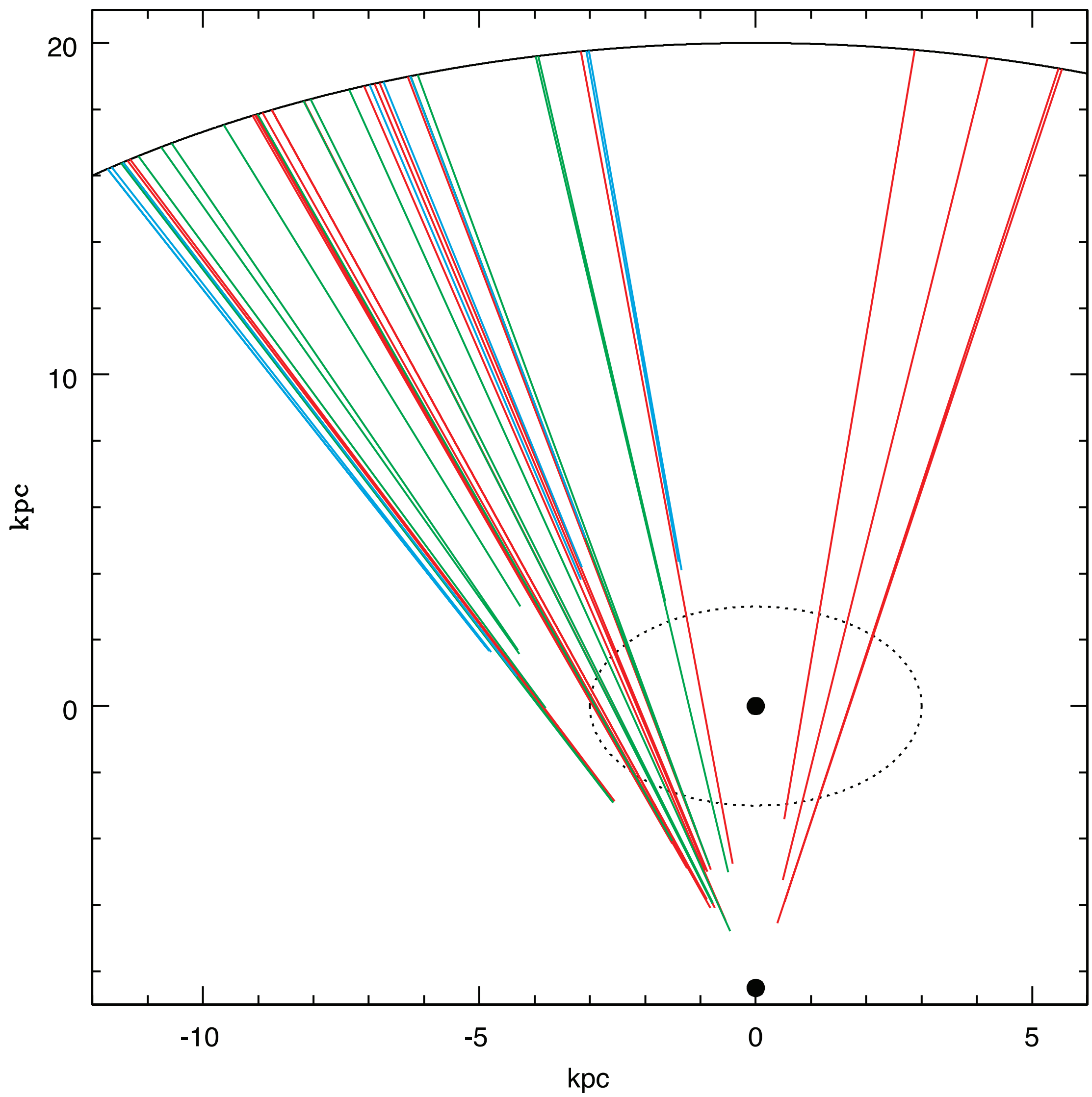

Fig. 3.—Lines of sight with line-averaged emissivities measured through the H II absorption method. The Galactic center is located at the origin and the Earth is located at (0, −8.5) kpc (IAU 1985 standard). The Galactic nonthermal emission is assumed to lie in a disk with radius 20 kpc (Ferrière 2001 and references therein), as indicated by the solid black line. Red lines represent lines of sight with emissivities $0.35\ \mathrm{K\ pc^{-1}} < \varepsilon < 0.52\ \mathrm{K\ pc^{-1}}$, green lines represent $0.52 < \varepsilon < 0.72$, and blue lines represent $0.72 < \varepsilon < 1.0$. Note that the axes have different scales and the view is from Galactic north down onto the plane. The dashed circle indicates the 3 kpc radius underdensity as modeled in § 6.

The paucity of data and the uncertain detection biases involved make modeling extremely difficult. Robust modeling based on these data may have to wait for the further development of low-frequency radio telescope fields; however, in this section we show one possible way in which such modeling might be undertaken.

The simplest possible model would be an axisymmetric disk of constant emissivity. The first undertaking is to see whether our data fit this model. As discussed in § 4.1, a regression fit is required due to the multivariate nature of the detection bias. We use the linear regression with survival analysis using the EM method,[7] which assumes a normal distribution of the nondetections around the fitted line. This technique is reviewed extensively in Isobe et al. (1986). The data were plotted as emissivity as a function of background column length.[8] A fit with a zero slope would confirm the constant emissivity model, and the intercept of the fit gives the value of the emissivity. The EM method regression with survival analysis gives a fit of $\varepsilon(D) = (-0.0109 \pm 0.0070)D + 0.5406 \pm 0.1654$, with ε in units of K pc^{-1} and D in kiloparsecs. This fit is marginally (1.5 σ) inconsistent with a zero slope, indicating that the constant emissivity model may be incorrect.

Of note in Figure 3 is the result that the averaged emissivities over path lengths originating on the far side of the Galactic center have higher values on average than path lengths originating closer to the observer. As a simple departure from the above model, an underdensity in the CR electron emissivity in the inner Galaxy could explain the lower emissivity values seen over longer path lengths.

Using the simple model of a cylinder 20 kpc in radius and 1 kpc thick, we calculate the mean emissivities one would expect to observe for a disk with uniform emissivity except for a central cylindrical region with zero emissivity. We try radii of 1, 2, 3, 4, 5, and 6 kpc for the central hole. EM method regression with

[7] We use the EM method as implemented in IRAF Revision 2.12.2. Data were also fitted using the Buckley-James method, with nearly identical results in all cases.

[8] When a source was measured in more than one field, the mean of the two measured values was used.

TABLE 7

EM Method Linear Regression with Survival Analysis Fits

R (kpc) (1)	Slope (K) (2)	Intercept (10^{-3} K pc^{-2}) (3)
0	-0.0109 ± 0.0070	0.5406 ± 0.1654
1	-0.0108 ± 0.0070	0.5401 ± 0.1652
2	-0.0091 ± 0.0069	0.5129 ± 0.1639
3	-0.0014 ± 0.0073	0.3646 ± 0.1742
4	0.0078 ± 0.0082	0.1903 ± 0.1946
5	0.0120 ± 0.0092	0.1322 ± 0.2188
6	0.0144 ± 0.0101	0.1145 ± 0.2394

Notes.—For the model fitting in § 6. Col. (1) is the size of the hypothesized central region devoid of emissivity. Cols. (2) and (3) are the slope and intercept of the fit, respectively.

survival analysis fits were performed, with the results detailed in Table 7. For a central emissivity hole of radii 0, 1, and 2 kpc, the slope fitted is not consistent with zero and is negative. For values of 4, 5, and 6, the slope is inconsistent with zero and positive. However, for the 3 kpc radius case, the fit is of the form $\varepsilon(D) = (-0.0014 \pm 0.0073)D + 0.3646 \pm 0.1742$, a fit that is consistent with zero slope, indicating an average emissivity of 0.3646 ± 0.1742 K pc^{-1} for regions outside the central underdensity. Figure 4 plots emissivity versus background path length for the observed data and the 3 kpc underdensity model.

Therefore, if a simple, constant-emissivity model is to be assumed, the best-fit model entails a region of zero emissivity approximately 3 kpc in radius and a constant emissivity of 0.36 ± 0.17 K pc^{-1} outside this radius. While we do not feel that the data warrant a more complex model, our best-fit model is clearly an oversimplification. In reality, for instance, the hole we have modeled is unlikely to be devoid of emissivity and would therefore represent an underdensity.

A literature search for works hypothesizing an underdensity in the Galactic CR emissivities in the inner Galaxy has found no theoretical or observational work indicating such a feature. The 408 MHz three-dimensional modeling of emissivity by Beuermann et al. (1985) has a slight underdensity at a radius of about 3 kpc but no central hole. Modeling by Webber (1983, 1993a, 1993b) based on CR nuclei observations and propagation models suggest a weak radial dependence (if any exists) of CRs and no central underdensity.

Although little work has been done suggesting the existence of a CR central underdensity, recent works (e.g., Lorimer 2004; Case & Bhattacharya 1998) suggest that there is a paucity of SNRs and pulsars in the inner several kiloparsecs. Lorimer (2004) invokes the current understanding of pulsar detection selection effects and applies these to the recent and extremely successful Parkes Multibeam pulsar survey to derive a pulsar radial density function that rises steeply from zero at the Galactic center, peaks around 3.5 kpc, and then falls exponentially [the functional form is $\rho(R) = R^N e^{-R/\sigma}$; Fig. 4 in Lorimer 2004]. Case & Bhattacharya (1998) use similar statistical methods, as well as a renormalization of the Σ-D (surface brightness–distance) relationship for shell SNRs to determine the density of SNRs as a function of galactocentric radius. A functional form similar to that of Lorimer (2004) is derived, with maximum density at ~5 kpc. In short, new works on the distribution of astrophysical objects that are derivatives of supernovae show a paucity in the few central kiloparsecs, as opposed to a maximum or flat density (e.g., Narayan 1987). If CR electrons are in fact closely associated with SNRs, the central underdensity indicated here would be consistent with an inner Galaxy underdensity of SNRs and pulsars. If the underdensity in CR emissivity indicated by our simple model is confirmed by future work, we note that CR propagation processes are not capable of filling the hole. This would be an important consideration in future modeling of CR propagation.

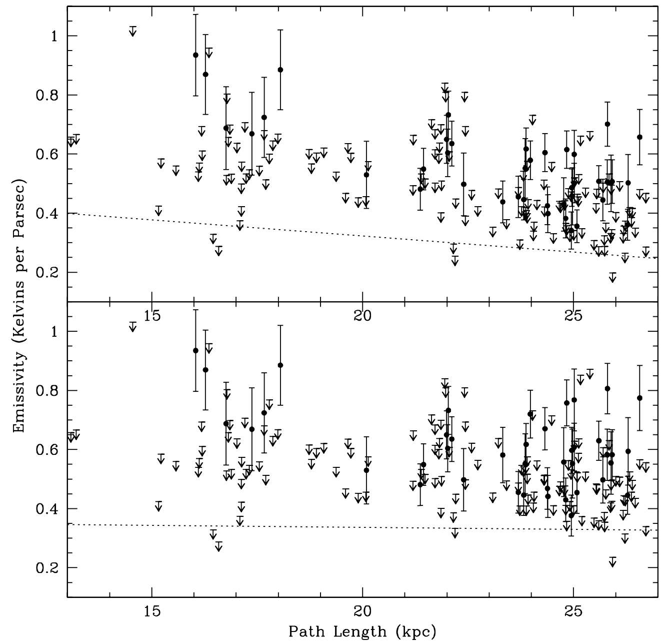

Fig. 4.—Emissivities derived from the inner Galaxy emissivity underdensity model. Values on the ordinate are integrated emissivities in K pc^{-1}. Values on the axis are the path length of the emissivity measurement in kiloparsecs. Detections are indicated with circles, 3 σ upper limits are indicated with arrows, and the dotted line represents the regression fit. *Top:* No central underdensity. The regression fit is marginally (1.5 σ) inconsistent with a uniform emissivity model. *Bottom:* 3 kpc central underdensity model. The regression fit is consistent with constant emissivity.

We point out that none of the lines of sight discussed here pass within ~1 kpc of the center of the Galaxy. Therefore, we are not hypothesizing a CR electron underdensity in the Galactic center. High star formation rates in the central 50 pc (e.g., Figer et al. 2004) and the diffuse nonthermal emission observed by LaRosa et al. (2005) indicate that the central few hundred parsecs may possess emissivities higher than the values measured in the disk of the Galaxy.

This uniform emissivity model with a central underdensity is a simple example of the possible ways in which the three-dimensional potential of H ii absorption features could be used. However, with only 42 lines of sight available, more complex models (e.g., emissivity models that have radial or azimuthal dependence) are underdetermined and will have to await further observations.

7. FURTHER WORK

It would be possible to increase the number of lines of sight available to this technique through further VLA observations in the first Galactic quadrant (the region extending into the fourth Galactic quadrant is inaccessible to the VLA) or by determining the distances to more of the H ii regions detected. This second option is difficult in the vicinity of the Galactic center, as the radial velocities of H ii regions are dominated by peculiar motions instead of the overall Galactic rotation in this region. It is also possible to calculate the brightness temperature of the column between the observer and the H ii region. However, a measurement of the total emissivity along a nearby line of sight is required. This measurement would have to be sensitive to the total flux (the *u-v* zero spacing) and yet have a resolution and frequency similar to the interferometer map. The resolution would need to be similar (within a factor of $\sim$3) because CR emissivity is sharply peaked along the Galactic plane ($<1^\circ$ typical size; Beuermann et al. 1985). Therefore, large beam sizes result in beam dilution and an underestimation of the brightness temperature. The frequency needs to be similar (50 MHz $\lesssim \nu \lesssim$ 150 MHz), as extrapolation over a large frequency range can cause large errors, and thermal emission and absorption change rapidly in this regime. Existing surveys, including the 408 MHz survey of Haslam et al. (1982), the 1420 MHz survey of Reich (1982), and the 34.5 MHz survey of Dwarkanth & Udaya Shankar (1990), were considered but do not have all the requirements to obtain a reasonable estimate of the total intensity. If such observations were to exist, the brightness temperature (and emissivity when distance is known) of the column in front of the H II region could be calculated, adding to the three-dimensional potential of this technique.

This technique may also hold some potential to break the degeneracy inherent in kinematic determinations of the distance to H II regions. Because these 74 MHz H II absorption detections are sensitive to the integrated brightness temperature of the column *behind* the absorbing medium (§ 3), the detections are biased toward closer H II regions. Therefore, the H II regions detected in this work are more likely "near" H II regions, i.e., the closer of the two degenerate values. This method was used by Brogan et al. (2003) to determine the distance to the Sgr D H II region. Alternatively, one could assume an emissivity along a line of sight and attempt to match the observed depth of the H II absorption feature in order to get a rough estimate of distance. However, background emissivity is not the only detection bias. The range of spatial sensitivity will select for H II regions on intrinsically larger angular scales, i.e., linearly larger and closer. An H II region that by chance had a strong CR electron source (i.e., an SNR) behind it would have a larger T_{bg} and therefore be easier to detect. For these reasons, this method should only be considered an indicator, not proof that any given H II region has the closer of the distance-degenerate values.

As a final note, we point out that the CR electrons detected here through interaction with the Galactic magnetic field are also detected in the soft γ-ray ($\sim$70 MeV; Webber 1990) regime via bremsstrahlung with interstellar gas. The radio measurement is essentially a line integration of CR density times magnetic field strength, while the γ-ray measurement is a line integration of CR density times interstellar gas density. Future radio measurements with emerging broadband low-frequency arrays such as the LWA will detect many more H II absorption features and constrain the spectrum of the synchrotron emissivity. Comparison of LWA and *Gamma-Ray Large Area Space Telescope* data should then allow one to break the degeneracy between magnetic field and cosmic-ray electron distribution inherent in radio observations alone, thereby providing direct information on the strength and spatial distribution of the Galactic magnetic field.

8. CONCLUSIONS

It has long been known that it is possible to use the large optical depth of H II regions at low radio frequencies to extract information concerning the three-dimensional distribution of CR emissivity without resorting to making assumptions about Galactic structure. Although H II regions have been observed in absorption at low frequencies before, the angular resolution and sensitivity required to detect more than a few nearby sources have only recently become available using the 74 MHz system on the VLA.

Ninety-two H II regions have been detected in absorption, and 42 of these have known distances, which are required to compute an emissivity. The measured emissivities are consistent with values expected from higher frequency extrapolation but are marginally inconsistent with a constant cosmic-ray emissivity model. An emissivity model consisting of an axisymmetric disk 20 kpc in radius with an emissivity of 0.36 ± 0.17 K pc^{-1} between 3 and 20 kpc and zero inside 3 kpc is a better fit with the data. Present data do not warrant more complex modeling (e.g., spiral arm structure and exponential disk). The increased resolution and surface brightness sensitivity expected of the next generation of low-frequency radio telescopes may be able to provide the increased number of lines of sight required for more complex modeling.

The authors thank C. Brogan of the University of Hawaii for allowing the use of previously collected data and assistance with data reduction, T. N. LaRosa for helpful comments, and the referee for very useful comments on selection effects and regression analysis. Basic research in radio astronomy at the NRL is supported by the Office of Naval Research. The National Radio Astronomy Observatory is a facility of the National Science Foundation operated under cooperative agreement by Associated Universities, Inc.

REFERENCES

Aharonian, F., et al. 2005, A&A, 432, L25
Beuermann, K., Kanbach, G., & Berkhuijsen, E. M. 1985, A&A, 153, 17
Braude, S. Y., Sokolov, K. P., & Zakharenko, S. M. 1994, Ap&SS, 213, 1
Brogan, C. L., Nord, M., Kassim, N., Lazio, J., & Anantharamaiah, K. 2003, Astron. Nachr. Suppl., 324, 17
Case, G. L., & Bhattacharya, D. 1998, ApJ, 504, 761
Cesarsky, C. J. 1980, ARA&A, 18, 289
Cornwell, T. J., & Perley, R. A. 1992, A&A, 261, 353
Duric, N. 1999, in ASP Conf. Ser. 168, New Perspectives on the Interstellar Medium, ed. A. R. Taylor, T. L. Landecker, & G. Joncas (San Francisco: ASP), 161
Dwarakanath, K. S., & Udaya Shankar, N. 1990, J. Astrophys. Astron., 11, 323
Erickson, W. C. 1984, J. Astrophys. Astron., 5, 55
Ferrière, K. M. 2001, Rev. Mod. Phys., 73, 1031
Figer, D. F., Rich, R. M., Kim, S. S., Morris, M., & Serabyn, E. 2004, ApJ, 601, 319
Gizani, N. A. B., Cohen, A., & Kassim, N. E. 2005, MNRAS, 358, 1061
Harwit, M. 1998, Astrophysical Concepts (New York: Springer)
Haslam, C. G. T., Stoffel, H., Salter, C. J., & Wilson, W. E. 1982, A&AS, 47, 1
Hess, V. 1919, Phys. Z., 13, 1084
Isobe, T., Feigelson, E. D., & Nelson, P. I. 1986, ApJ, 306, 490
Jones, T. W., et al. 1998, PASP, 110, 125
Kassim, N. E. 1987, Ph.D. thesis, Univ. Maryland
———. 1988, ApJS, 68, 715
Kassim, N. E., Perley, R. A., Erickson, W. C., & Dwarakanath, K. S. 1993, AJ, 106, 2218
Koyama, K., Petre, R., Gotthelf, E. V., Hwang, U., Matsuura, M., Ozaki, M., & Holt, S. S. 1995, Nature, 378, 255
Lane, W. M., Cohen, A. S., Kassim, N. E., Lazio, T. J. W., Perley, R. A., Cotton, W. D., & Greisen, E. W. 2005, Radio Sci., 40, 5
LaRosa, T. N., Brogan, C. L., Shore, S. N., Lazio, T. J., Kassim, N. E., & Nord, M. E. 2005, ApJ, 626, L23
Lisenfeld, U., & Völk, H. J. 2000, A&A, 354, 423
Longair, M. S. 1990, in Low-Frequency Astrophysics from Space, ed. N. E. Kassim & K. W. Weiler (Berlin: Springer), 227
Lorimer, D. R. 2004, in IAU Symp. 218, Young Neutron Stars and Their Environments, ed. F. Camilo & B. M. Gaensler (San Francisco: ASP), 105
Narayan, R. 1987, ApJ, 319, 162

Nord, M. E. 2005, Ph.D. thesis, Univ. New Mexico
Nord, M. E., Lazio, T. J. W., Kassim, N. E., Hyman, S. D., LaRosa, T. N., Brogan, C. L., & Duric, N. 2004, AJ, 128, 1646
Paladini, R., Burigana, C., Davies, R. D., Maino, D., Bersanelli, M., Cappellini, B., Platania, P., & Smoot, G. 2003, A&A, 397, 213
Paladini, R., Davies, R. D., & DeZotti, G. 2004, MNRAS, 347, 237
Platania, P., Burigana, C., Maino, D., Caserini, E., Bersanelli, M., Cappellini, B., & Mennella, A. 2003, A&A, 410, 847
Rand, R. J., & Kulkarni, S. R. 1989, ApJ, 343, 760
Reich, W. 1982, A&AS, 48, 219
Reich, W., Reich, P., & Fuerst, E. 1990, A&AS, 83, 539
Rockstroh, J. M., & Webber, W. R. 1978, ApJ, 224, 677
Scheuer, P. A. G., & Ryle, M. 1953, MNRAS, 113, 3
Webber, W. R. 1983, in Composition and Origin of Cosmic Rays, ed. M. M. Shapiro (Dordrecht: Reidel), 25
———. 1990, in Low-Frequency Astrophysics from Space, ed. N. E. Kassim & K. W. Weiler (Berlin: Springer), 217
———. 1993a, ApJ, 402, 185
———. 1993b, ApJ, 402, 188
———. 1998, ApJ, 506, 329